Advanced Composites and Hybrid Materials (2021) 4:733–742
https://doi.org/10.1007/s42114-021-00291-4

ORIGINAL RESEARCH

Al^{3+}-doped $FeNb_{11}O_{29}$ anode materials with enhanced lithium-storage performance

Jinping Huang[1] · Qing Chen[1] · Shuaifeng Chen[1] · Lijie Luo[1] · Jianbao Li[1] · Chunfu Lin[2] · Yongjun Chen[1]

Received: 13 April 2021 / Revised: 16 June 2021 / Accepted: 17 June 2021 / Published online: 26 June 2021

Abstract

$FeNb_{11}O_{29}$ has a high theoretical capacity as a potential anode material for lithium-ion batteries; however, the practical capacity of $FeNb_{11}O_{29}$ reported was unsatisfactory. In this study, a simple and efficient Al^{3+}-doping technique was demonstrated to improve the electrochemical performance of $FeNb_{11}O_{29}$ successfully. The influences of the Al^{3+} doping amount were investigated. It was found that the crystal structure of $FeNb_{11}O_{29}$ could be preserved when a suitable amount of Al^{3+} was added, and that $Al_{0.2}Fe_{0.8}Nb_{11}O_{29}$ demonstrated better electrochemical performance than $FeNb_{11}O_{29}$ because the structure of $Al_{0.2}Fe_{0.8}Nb_{11}O_{29}$ is more stable. At 0.1C, $Al_{0.2}Fe_{0.8}Nb_{11}O_{29}$ possessed a high reversible capacity of 318 mAh g^{-1} with an initial-cycle Coulombic efficiency of 95.0%. $Al_{0.2}Fe_{0.8}Nb_{11}O_{29}$ exhibited outstanding cycling stability with capacity retention of 92.9% at 10C over after 1000 cycles. Moreover, A $LiFePO_4/Al_{0.2}Fe_{0.8}Nb_{11}O_{29}$ full cell was prepared successfully with a discharge capacity of 206 mAh g^{-1}. The full cell exhibited good cycling stability showing the capacity retention of 84.2% over after 200 cycles at 1C and 89.8% over after 1000 cycles at 5C, respectively. This work suggests that $Al_{0.2}Fe_{0.8}Nb_{11}O_{29}$ has great application prospects in lithium-ion batteries.

Keywords $FeNb_{11}O_{29}$ · Al^{3+} doping · Anode material · Lithium-ion battery · Electrochemical performance

1 Introduction

Lithium-ion batteries (LIBs) are regarded as a kind of green power with good cycling performance and high energy density [1–5], which have become one of the hottest research topics these years. At present, the LIB anodes are normally composed of graphite-like materials because of their inexpensive and high theoretical capacity (372 mAh g^{-1}) [6]. However, due to the relatively low rate capability, it is easy to cause the formation of thick solid electrolyte interface (SEI) layers and the growth of lithium dendrites which are hindering the application of graphite-anode materials [7]. $Li_4Ti_5O_{12}$ has been explored to overcome these disadvantages [8–10], which could avoid the formation of thick SEI layers and display good safety performance. However, the low theoretical capacity of $Li_4Ti_5O_{12}$ (175 mAh g^{-1}) limits its practical application. Therefore, it is necessary to explore novel anode material substitutes with similar advantages to $Li_4Ti_5O_{12}$ but much higher theoretical capacities.

Recently, niobium oxide-based materials have attracted great attention due to their high theoretical capacities (374–403 mAh g^{-1}) which are benefitted from the Nb^{4+}/Nb^{5+} and Nb^{3+}/Nb^{4+} multi-electron redox couples. To date, a series of niobium oxide-based anode materials have been explored by our group, such as $Nb_{25}O_{62}$ [11], $MoNb_{12}O_{33}$ [12], $AlNb_{11}O_{29}$ [13], $Al_{0.5}Nb_{24.5}O_{62}$ [14], $CrNb_{11}O_{29}$ [15], $Mg_2Nb_{34}O_{87}$ [16], $GaNb_{11}O_{29}$ [17], $TiNb_{24}O_{62}$ [18], and $ZrNb_{24}O_{62}$ [19]. $FeNb_{11}O_{29}$ [20], $W_3Nb_{14}O_{44}$ [21], and $K_2Nb_8O_{21}$ [22] were also found by other researchers to be good anode material candidates. In particularly, $FeNb_{11}O_{29}$ has a theoretical capacity of 400 mAh g^{-1} owing to the existence of three Fe^{2+}/Fe^{3+}, Nb^{4+}/Nb^{5+}, and Nb^{3+}/Nb^{4+}

✉ Lijie Luo
luolijie4567@163.com

✉ Chunfu Lin
linchunfu@qdu.edu.cn

✉ Yongjun Chen
chenyj99@163.com

[1] School of Materials Science and Engineering, Key Lab of Advanced Materials of Tropical Island Resources, Ministry of Education, Hainan University, Haikou 570228, China

[2] Institute of Materials for Energy and Environment, School of Materials Science and Engineering, Qingdao University, Qingdao 266071, China

redox couples (each formula unit of $FeNb_{11}O_{29}$ could transfer 23 electrons) [20]. However, the practical capacities of $FeNb_{11}O_{29}$ reported were only 168–273 mAh g^{-1} at 0.1C [20, 23–25]. Therefore, it is of great significance to enhance the specific capacity of $FeNb_{11}O_{29}$ for practical applications.

Currently, rare works were reported for improving the electrochemical performance of $FeNb_{11}O_{29}$. Zheng et al. increased the specific capacity of $FeNb_{11}O_{29}$ from 226 to 273 mAh g^{-1} at 0.1C by fabricating $FeNb_{11}O_{29}$ nanotubes, and the initial-cycle Coulombic efficiency was improved from 75.9 to 90.1% [20]. Lou et al. prepared Cr^{3+}-doped $FeNb_{11}O_{29}$ ($Cr_{0.2}Fe_{0.8}Nb_{11}O_{29}$) with a specific capacity of 254 mAh g^{-1} [24]. Lou et al. further enhanced the specific capacity of $FeNb_{11}O_{29}$ to 270 mAh g^{-1} through generating oxygen vacancies [25]. In electrochemical experiments, there are common methods used to improve the electrochemical performance of electrode materials, such as carbon composite [26–28], plasmonization [29, 30], surfactant-assisted process [31], and nanosizing [32, 33]. It is believed that doping is also a common and efficient method to improve the cycling performance and rate capability of electrode materials because of its easy operation, low-consumption, and large-scale production [34–45]. Aluminum (Al) has been paid more and more attention as a substitute for various electrode materials owning to its abundant in earth, nontoxic and light characteristics [46, 47]. It has been found that Al doping could enhance the electrochemical performance of anode materials significantly because the strong Al–O bonds favor the structural stability [48–50]. Therefore, in this study, $FeNb_{11}O_{29}$ materials were also modified by doping with Al. The experimental results showed that Al^{3+} successfully and partically replaced Fe^{3+} and that the obtained $Al_{0.2}Fe_{0.8}Nb_{11}O_{29}$ materials preserved the crystal structure, grain size and morphology of $FeNb_{11}O_{29}$. Better structural stability was achieved due to the strong Al–O bonds, which greatly enhanced the electrochemical performance of $FeNb_{11}O_{29}$.

2 Experimental

2.1 Material synthesis

The $Al_xFe_{1-x}Nb_{11}O_{29}$ ($x = 0.1$, 0.2, and 0.3) materials were synthesized via a simple solid-state reaction method by using Nb_2O_5 (Sinopharm, 99.9%), Al_2O_3 (Aladdin, 99.0%), and Fe_2O_3 (Aladdin, 99.0%) as the raw materials. Nb_2O_5, Fe_2O_3, and different contents of Al_2O_3 were mixed in ethanol, which were then ground in a high-energy ball-milling machine (SPEX 8000 M, USA) for 4 h. After drying, the ball-milled mixtures were sintered in a muffle furnace at 1300 °C in air for 4 h, forming $Al_xFe_{1-x}Nb_{11}O_{29}$ materials ($x = 0.1$, 0.2, and 0.3). For comparison, undoped $FeNb_{11}O_{29}$ counterpart was also fabricated with a similar procedure and without the use of Al_2O_3.

2.2 Material characterization

The crystalline structures of the obtained samples were characterized by X-ray diffraction (XRD) on an X-ray diffractometer (German Bruker D8). The phase purity and lattice parameters were determined by Rietveld refinements, which were conducted by using the GSAS program with the EXPGUI interface [51, 52]. Morphologies, particle sizes, and microstructures of synthesized samples were recorded by scanning electron microscopy (SEM, S-4800), high-resolution transmission electron microscopy (HRTEM, Tecnai G2 F20 S-TWIN, FEI), and energy dispersive X-ray spectrometer (EDX) mapping. The specific surface areas of the samples were determined by nitrogen adsorption/desorption device (ASAP 2460).

2.3 Half-cell measurement

The electrochemical performance of $Al_xFe_{1-x}Nb_{11}O_{29}$/Li ($x = 0$, 0.1, and 0.2) was evaluated by employing CR2016-type coin cells. Firstly, the working electrodes were prepared by mixing 70 wt% of $Al_xFe_{1-x}Nb_{11}O_{29}$ (active material) powder, 20 wt% of conductive carbon (Super P, battery level), and 10 wt% of polyvinylidene fluoride (PVDF) binder, thoroughly mixed in N-methylpyrrolidone (NMP) to form a homogeneous slurry. After stirring the slurry for 8 h, the slurry was coated onto a copper foil evenly. The mass loading of $Al_xFe_{1-x}Nb_{11}O_{29}$ was ~ 1.0 mg cm^{-2}. Then, the coated foils were dried in a vacuum oven at 120 °C for 10 h and were cut into a circular plate with a diameter of 10 mm. The CR2016 coin cells were assembled in a glove box filled with argon gas ($O_2/H_2O < 0.1$ ppm) and consisted of an above as-prepared electrode, a Li foil that acted as counter and reference electrodes, a microporous polypropylene film (Celgard 2325) and electrolyte containing 1 M $LiPF_6$ (DAN VEC) in a mixed solvent of ethylene carbonate (EC), dimethyl carbonate (DMC), and diethylene carbonate (DEC) with a volume ratio of 1:1:1. Galvanostatic discharge–charge measurements and galvanostatic intermittent titration technique (GITT) tests were performed on a Neware battery tester. Cyclic voltammetry (CV) measurements were conducted on a CHI660E electrochemical workstation. The electrochemical performance was examined within 3.0–0.8 V. To prepare the $Al_xFe_{1-x}Nb_{11}O_{29}$ electrodes for ex situ XRD, the half cells at different states of discharge/charge were disassembled in the glove box, followed by washing the obtained $Al_xFe_{1-x}Nb_{11}O_{29}$ electrodes by dimethyl carbonate.

2.4 Full-cell measurement

Full cells (CR2032-type coin cells) were assembled with the as-prepared $Al_{0.2}Fe_{0.8}Nb_{11}O_{29}$ as the anode and commercial $LiFePO_4$ as the cathode. Similarly, $LiFePO_4$ powder, conductive carbon (Super P), and PVDF with a weight ratio of 7:2:1 were thoroughly mixed in N-methylpyrrolidone (NMP) to form a homogeneous slurry. Then, the slurry was spread evenly on an Al foil and made into a circular plate with a diameter of 10 mm. The $LiFePO_4$:$Al_{0.2}Fe_{0.8}Nb_{11}O_{29}$ weight ratio was fixed to be 2:1. Galvanostatic discharge–charge measurements were performed within 1.0–2.5 V.

3 Results and discussion

Figure 1 shows the XRD patterns of $FeNb_{11}O_{29}$ and $Al_xFe_{1-x}Nb_{11}O_{29}$ ($x = 0.1$, 0.2, and 0.3), and the corresponding Rietveld-refined data are demonstrated in Table S1. It can be seen that the XRD patterns of $Al_xFe_{1-x}Nb_{11}O_{29}$ ($x = 0.1$ and 0.2) completely match those of $FeNb_{11}O_{29}$ with an orthorhombic shear ReO_3 crystal structure and *Amma* space group (JCPDS#22–0352; Fig. S1). No other phases (such as Nb_xO_y or Fe_2O_3) are observed. Table S1 shows that the weighted profile residual (R_{wp}) values of the samples are small (about 10%), revealing that the Rietveld refinement results are credible. The fractional atomic parameters of $FeNb_{11}O_{29}$ and $Al_{0.2}Fe_{0.8}Nb_{11}O_{29}$ are shown in Tables S2 and S3, respectively. Since the ionic radius of Al^{3+} is smaller than Fe^{3+}, it is reasonable that the lattice parameters get smaller [45, 53]. It is noteworthy that the *b* values of $Al_xFe_{1-x}Nb_{11}O_{29}$ ($x = 0.1$ and 0.2) are larger than that of the previous $Ti_2Nb_{10}O_{29}$ ($b = 3.805$ Å) reported [54], suggesting the existence of larger gap sites in $Al_xFe_{1-x}Nb_{11}O_{29}$ that are more conducive to Li^+ diffusion. However, when the Al^{3+} doping amount further increases ($x = 0.3$), the crystal structure of orthorhombic shear ReO_3 changes, indicating that the allowable Al^{3+} doping amount is limited (i.e., $x \leq 0.2$; Fig. 1) [53, 55].

Figure 2 illustrates the SEM images of $FeNb_{11}O_{29}$ and $Al_xFe_{1-x}Nb_{11}O_{29}$ ($x = 0.1$, 0.2, and 0.3). It can be observed that all the samples consist of grains which possess a platelet morphology. The BET-specific surface area of $Al_{0.2}Fe_{0.8}Nb_{11}O_{29}$ is 0.27 $m^2\ g^{-1}$ (Fig. S2b), which is slightly smaller than $FeNb_{11}O_{29}$ (0.24 $m^2\ g^{-1}$; Fig. S2a), verifying that $Al_{0.2}Fe_{0.8}Nb_{11}O_{29}$ and $FeNb_{11}O_{29}$ have similar particle sizes. Thus, there are almost little influences on the grain morphology and size of $FeNb_{11}O_{29}$ through the Al^{3+} doping.

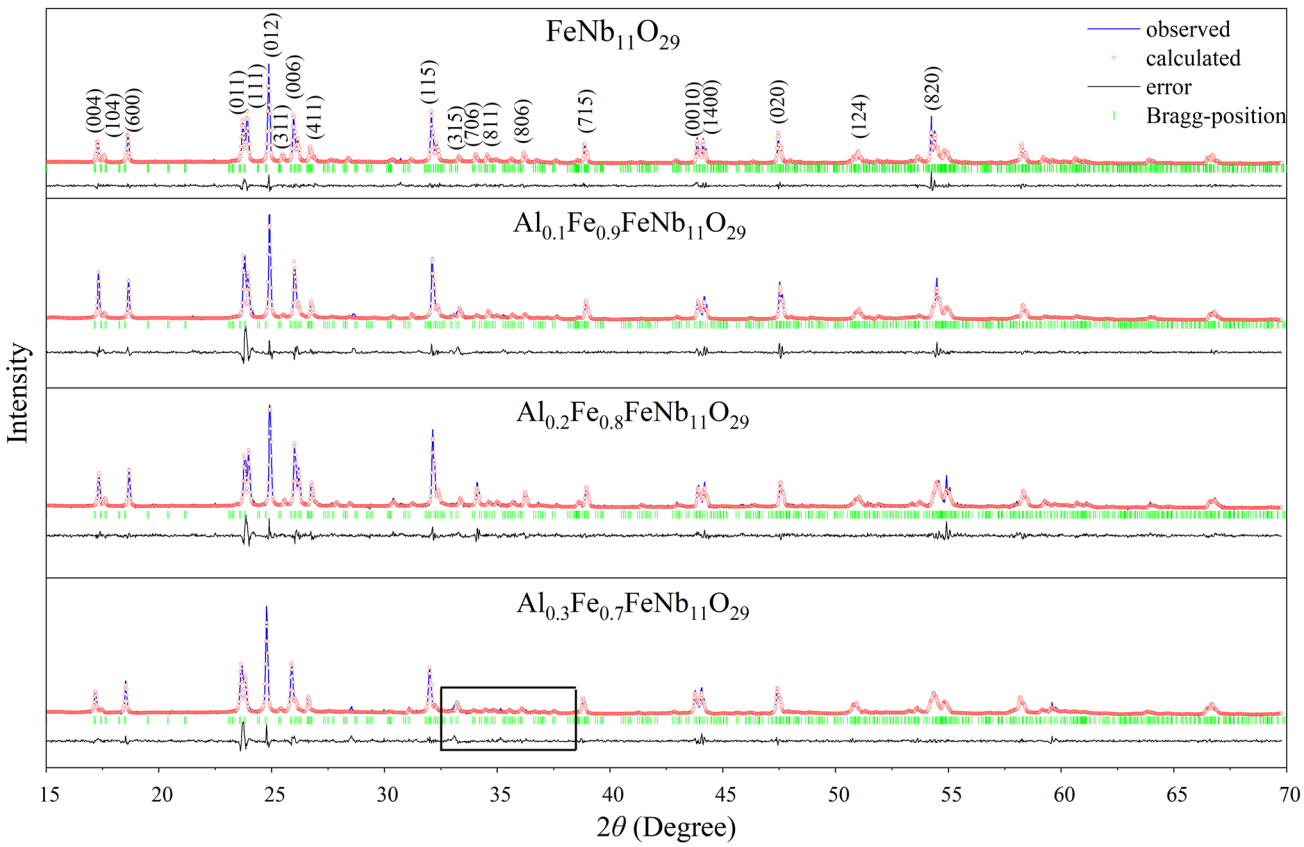

Fig. 1 XRD patterns and Rietveld refinement results of $FeNb_{11}O_{29}$ and $Al_xFe_{1-x}Nb_{11}O_{29}$ ($x = 0.1$, 0.2, and 0.3) materials

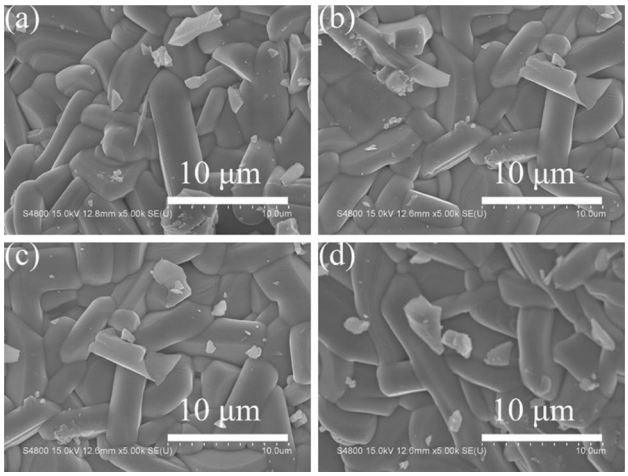

Fig. 2 SEM images of **a** $FeNb_{11}O_{29}$, **b** $Al_{0.1}Fe_{0.9}Nb_{11}O_{29}$, **c** $Al_{0.2}Fe_{0.8}Nb_{11}O_{29}$, and **d** $Al_{0.3}Fe_{0.7}Nb_{11}O_{29}$

Figure 3 depicts the HRTEM images of $FeNb_{11}O_{29}$ (Fig. 3a) and $Al_{0.2}Fe_{0.8}Nb_{11}O_{29}$ (Fig. 3b), revealing their lattice fringes of 0.351 and 0.349 nm, respectively, which correspond to (311) planes. The interplanar spacing contraction in $Al_{0.2}Fe_{0.8}Nb_{11}O_{29}$ may be due to the smaller ionic radius of Al^{3+} in comparison with Fe^{3+}. The results further verify that the crystal structure of $FeNb_{11}O_{29}$ does not change after doping with a suitable amount of Al^{3+}, which are also consistent with the XRD characterization. The EDS elemental mapping images shown in Fig. 3c, d indicate that Fe, Nb, and O elements, and Al, Fe, Nb, and O elements, are uniformly distributed in $FeNb_{11}O_{29}$ and $Al_{0.2}Fe_{0.8}Nb_{11}O_{29}$ materials, respectively, further confirming the successful doping of Al^{3+} into $FeNb_{11}O_{29}$.

In order to understand the electrochemical mechanism of $FeNb_{11}O_{29}$ and $Al_{0.2}Fe_{0.8}Nb_{11}O_{29}$, CV tests with different scanning speeds were carried out on the $FeNb_{11}O_{29}$ and

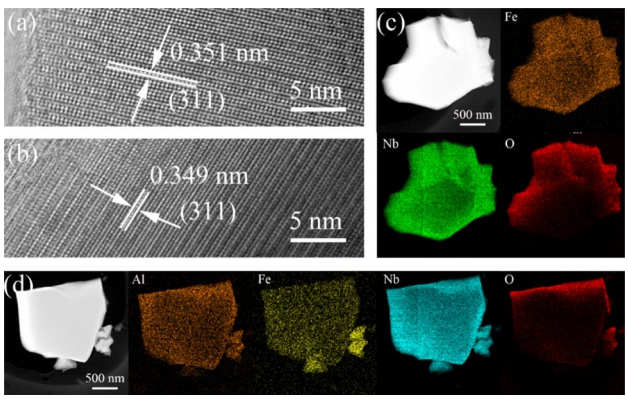

Fig. 3 HRTEM images of **a** $FeNb_{11}O_{29}$ and **b** $Al_{0.2}Fe_{0.8}Nb_{11}O_{29}$. EDX elemental mapping images of **c** $FeNb_{11}O_{29}$ and **d** $Al_{0.2}Fe_{0.8}Nb_{11}O_{29}$

$Al_{0.2}Fe_{0.8}Nb_{11}O_{29}$-made electrodes under a potential window of 3.0–0.8 V. Figure 4a, b show the first four-cycle CV curves of these two electrodes tested at 0.2 mV s^{-1}. The redox peak of the $FeNb_{11}O_{29}$ electrode can be attributed to Nb^{3+}/Nb^{4+}, Nb^{4+}/Nb^{5+}, and Fe^{2+}/Fe^{3+} redox pairs (Fig. 4a). In particular, the Nb^{3+}/Nb^{4+} peak is at ~ 1.10/1.30 V, the Nb^{4+}/Nb^{5+} peak is at ~ 1.53/1.72 V, and the Fe^{2+}/Fe^{3+} peak is at ~ 2.36 V. The average working potential of $FeNb_{11}O_{29}$ is calculated to be ~ 1.61 V. For the $Al_{0.2}Fe_{0.8}Nb_{11}O_{29}$ electrode (Fig. 4b), the Nb^{3+}/Nb^{4+} peak is at ~ 1.10/1.30 V, the Nb^{4+}/Nb^{5+} peak is at ~ 1.59/1.72 V, and the Fe^{2+}/Fe^{3+} peak is at ~ 2.35 V. The average working potential of $Al_{0.2}Fe_{0.8}Nb_{11}O_{29}$ is also ~ 1.61 V. Clearly, $Al_{0.2}Fe_{0.8}Nb_{11}O_{29}$ and $FeNb_{11}O_{29}$ have a very similar CV characteristic, hinting the similar reaction kinetics.

Figure 4c, d illustrate the CV curves of $FeNb_{11}O_{29}$ and $Al_{0.2}Fe_{0.8}Nb_{11}O_{29}$ electrodes at different scanning speeds, respectively. It can be seen that with the increase of the scanning speeds, the current values of the redox front increase in both $FeNb_{11}O_{29}$ and $Al_{0.2}Fe_{0.8}Nb_{11}O_{29}$ electrodes. However, compared with $FeNb_{11}O_{29}$, $Al_{0.2}Fe_{0.8}Nb_{11}O_{29}$ has a stronger redox front, revealing that Al^{3+} doping enables better electrochemical-kinetics behavior.

The constant current discharge–charge curves of the $FeNb_{11}O_{29}$ and $Al_{0.2}Fe_{0.8}Nb_{11}O_{29}$ electrodes are demonstrated in Fig. 5a, b, respectively. Each discharge–charge curve was divided into three regions: a short slope at 3.0–1.7 V, a short platform at 1.7–1.6 V, and a long slope at 1.6–0.8 V. Solid solution reactions occur in the first and third regions, and a two-phase reaction occurs in the second region. It can be found that the $FeNb_{11}O_{29}$ electrode has a reversible capacity of 262 mAh g^{-1} with an initial-cycle Coulombic efficiency of 91.1%, while the $Al_{0.2}Fe_{0.8}Nb_{11}O_{29}$ electrode has an enhanced reversible capacity of 318 mAh g^{-1} with an initial-cycle Coulombic efficiency of 95.0%. Table 1 lists the electrochemical performance of the $Al_{0.2}Fe_{0.8}Nb_{11}O_{29}$ and M-Nb–O materials reported in literatures. It is clear that the capacity of $Al_{0.2}Fe_{0.8}Nb_{11}O_{29}$ is higher than those of most reported M-Nb–O materials (except for $MoNb_{12}O_{33}$ and $Mg_2Nb_{34}O_{87}$), and the initial-cycle Coulombic efficiency is only lower than $GaNb_{11}O_{29}$. It is believed that the relatively high working potential of $Al_{0.2}Fe_{0.8}Nb_{11}O_{29}$ (~ 1.61 V) results in the less formation of SEI layer during the electrochemical reaction process, which reduces the consumption of lithium ions and leads to the high initial-cycle Coulombic efficiency [7].

Figure 5c, d show the discharge–charge curves of the $FeNb_{11}O_{29}$ and $Al_{0.2}Fe_{0.8}Nb_{11}O_{29}$ electrodes at different current density, respectively. When the current density increases from 0.1 to 10C, the specific capacity of $FeNb_{11}O_{29}$ decreases from 262 to 104 mAh g^{-1}, while that of $Al_{0.2}Fe_{0.8}Nb_{11}O_{29}$ electrode decreases from 318 to 134 mAh g^{-1}. Figure 5e demonstrates the rate capabilities of

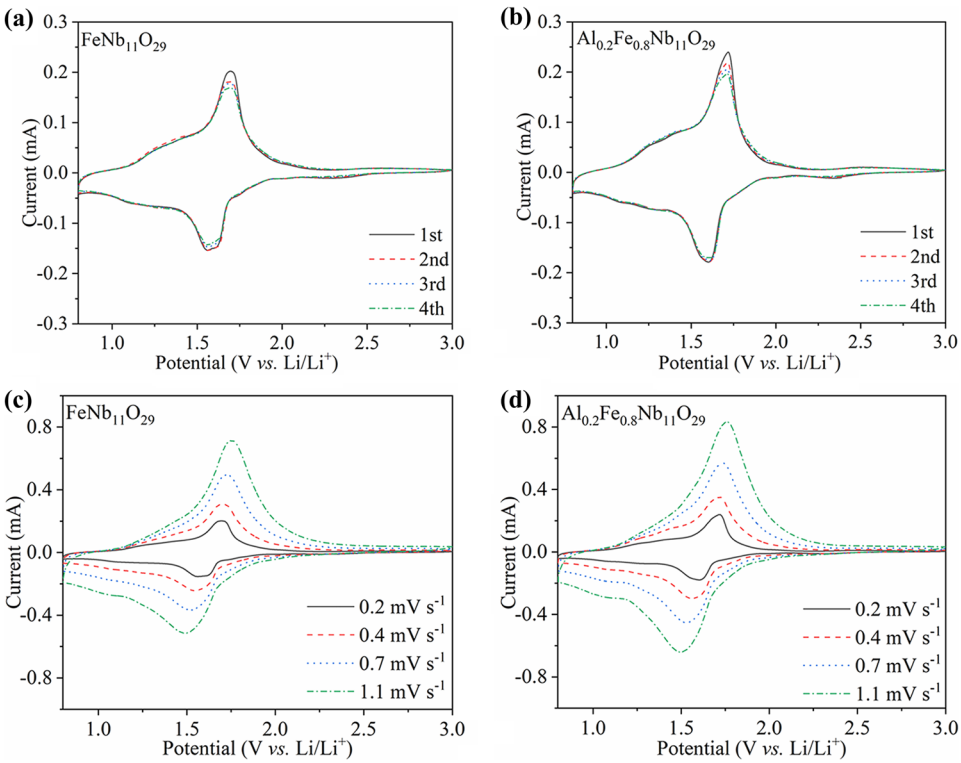

Fig. 4 The first four CV cycles of **a** $FeNb_{11}O_{29}$ electrode and **b** $Al_{0.2}Fe_{0.8}Nb_{11}O_{29}$ electrode at 0.2 mV s^{-1}. The CV curves of **c** $FeNb_{11}O_{29}$ electrode and **d** $Al_{0.2}Fe_{0.8}Nb_{11}O_{29}$ electrode at different scan rates

the $FeNb_{11}O_{29}$ and $Al_{0.2}Fe_{0.8}Nb_{11}O_{29}$ electrodes at various current densities. Both the specific capacities of the $FeNb_{11}O_{29}$ and $Al_{0.2}Fe_{0.8}Nb_{11}O_{29}$ electrodes reduce with increasing the current density. It can also be found that the specific capacity of the $Al_{0.2}Fe_{0.8}Nb_{11}O_{29}$ electrode at 10C is even higher than the $FeNb_{11}O_{29}$ electrode at 5C. Therefore, the $Al_{0.2}Fe_{0.8}Nb_{11}O_{29}$ electrode has achieved a better rate capability. This high rate capability is due to the fact that $Al_{0.2}Fe_{0.8}Nb_{11}O_{29}$ has a stronger redox front. Moreover, Fig. S3a, b illustrate the discharge–charge curves of the $Al_{0.1}Fe_{0.9}Nb_{11}O_{29}$ electrode. The $Al_{0.1}Fe_{0.9}Nb_{11}O_{29}$ electrode also exhibits an improved specific capacity (272 mAh g^{-1}) in comparison with the undoped $FeNb_{11}O_{29}$ electrode, but lower than that of the $Al_{0.2}Fe_{0.8}Nb_{11}O_{29}$ electrode. This result indicates that more Al^{3+} doping has a more significant effect on improving the reversible capacity of $FeNb_{11}O_{29}$.

Figure 5f illustrates the cycling performance of the $FeNb_{11}O_{29}$ and $Al_{0.2}Fe_{0.8}Nb_{11}O_{29}$ electrodes at a current density of 10C. After 1000 cycles, the capacity retention rate of $Al_{0.2}Fe_{0.8}Nb_{11}O_{29}$ is 92.9%, which is obviously higher than that of $FeNb_{11}O_{29}$ (85.8%), proving that Al^{3+} doping is very beneficial to the cycling stability of $FeNb_{11}O_{29}$. The excellent cycling stability is due to the fact that $Al_{0.2}Fe_{0.8}Nb_{11}O_{29}$ owns excellent structural stability.

To study the Li^+ diffusivity of the $FeNb_{11}O_{29}$ and $Al_{0.2}Fe_{0.8}Nb_{11}O_{29}$ electrodes, the GITT tests were employed at room temperature (Fig. 6). Figure 6a, b record the initial GITT curves of the $FeNb_{11}O_{29}$ and $Al_{0.2}Fe_{0.8}Nb_{11}O_{29}$ electrodes at 0.1C, respectively. The diffusion coefficient of $Li^+(D_{Li^+})$ can be calculated according to Fick's second law (Eq. (1)):

$$D_{Li^+} = \frac{4}{\pi}\left(\frac{m_B V_m}{M_B S}\right)^2 \left(\frac{\Delta E_s}{\tau\left(dE_\tau/d\sqrt{\tau}\right)}\right)^2 \left(\tau << \frac{L^2}{D^2}\right) \quad (1)$$

$$D_{Li^+} = \frac{4}{\pi\tau}\left(\frac{m_B V_m}{M_B S}\right)^2 \left(\frac{\Delta E_s}{\Delta E_\tau}\right)^2 \left(\tau << \frac{L^2}{D^2}\right) \quad (2)$$

where M_B and m_B are the molar mass and unit mass of the active material, respectively; V_m stands the molar volume of the active material; S stands the polar area; τ is titration time; L stands for the diffusion length; and ΔE_S and ΔE_τ represent the change of equilibrium potential and the change in potential during a single-step titration (Fig. S4a, b), respectively. Since there is a linear relationship between $\tau^{0.5}$ and the potential during the single-step titration (Fig. S4c, d), Eq. (1) can be simplified as Eq. (2). Figure 6c, d describe how the calculated D_{Li^+} values vary with the potential. During the Li^+ insertion process, the calculated D_{Li^+} values of the $FeNb_{11}O_{29}$ electrode are 8.03×10^{-13}–3.71×10^{-11} cm^2 s^{-1} with an average value of 1.47×10^{-11} cm^2 s^{-1}, while the $Al_{0.2}Fe_{0.8}Nb_{11}O_{29}$ electrode has calculated D_{Li^+} values of 1.67×10^{-12}–3.41×10^{-11} cm^2 s^{-1} with an average value of 1.76×10^{-11} cm^2 s^{-1}. For the Li^+ extraction process,

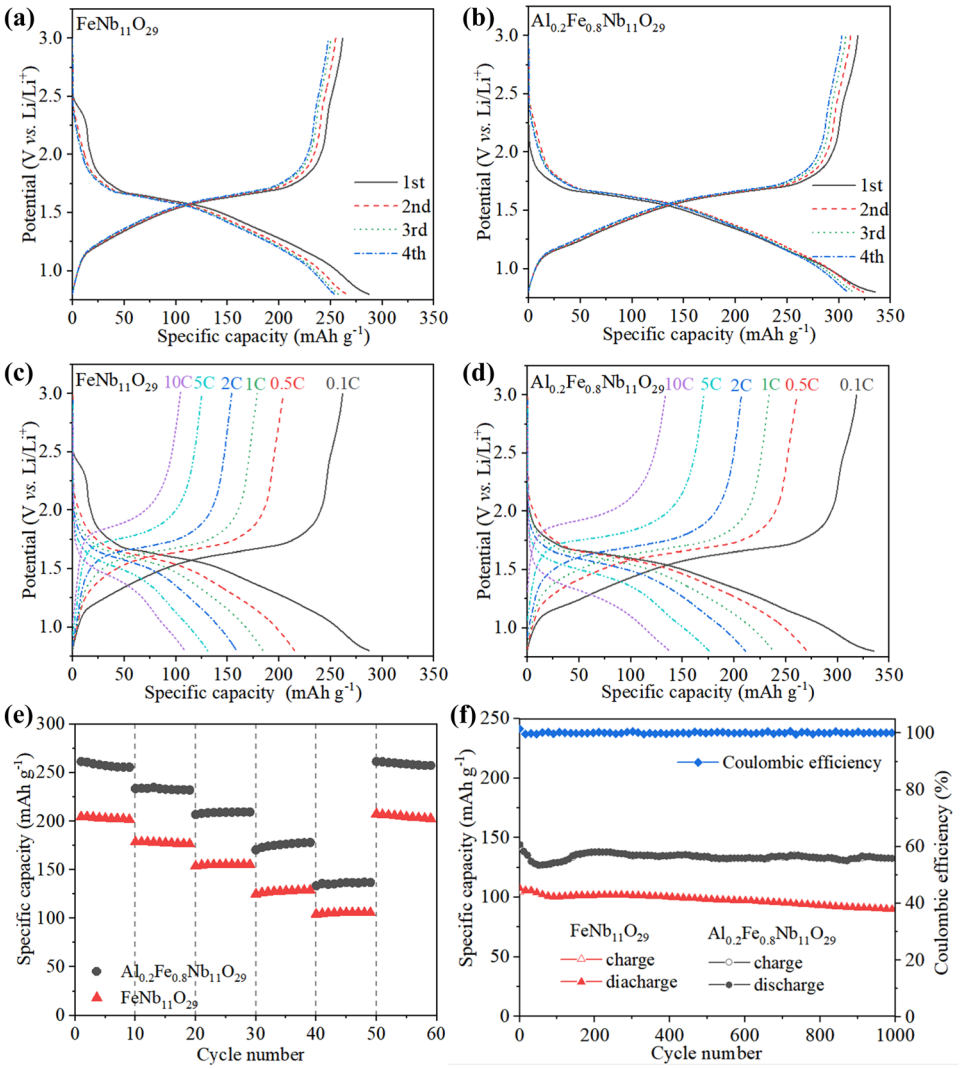

Fig. 5 Electrochemical performance of $FeNb_{11}O_{29}$ and $Al_{0.2}Fe_{0.8}Nb_{11}O_{29}$ electrodes: **a**, **b** discharge–charge curves at 0.1C, **c**, **d** discharge–charge curves at 0.1–10C, **e** rate capabilities, and **f** cycling stability at 10C after 1000 cycles and Coulombic efficiency of $Al_{0.2}Fe_{0.8}Nb_{11}O_{29}$

the calculated D_{Li^+} values of the $FeNb_{11}O_{29}$ electrode are 3.95×10^{-12}–1.83×10^{-11} $cm^2\ s^{-1}$ with an average value of 1.28×10^{-11} $cm^2\ s^{-1}$, while the $Al_{0.2}Fe_{0.8}Nb_{11}O_{29}$ electrode has calculated D_{Li^+} values of 7.24×10^{-12}–2.60×10^{-11} $cm^2\ s^{-1}$ with an average value of 1.64×10^{-11} $cm^2\ s^{-1}$. These similar Li^+ diffusivity can be explained by the similar lattice parameters and unit-cell volumes of the two materials (Table S1).

Table 1 Electrochemical performance of $Al_{0.2}Fe_{0.8}Nb_{11}O_{29}$ compared with M-Nb–O materials reported

Material	Initial-cycle reversible capacity (mAh g^{-1})	Initial-cycle Coulombic efficiency (%)	Reference
$Nb_{12}O_{29}$	289	/	[11]
$Nb_{25}O_{62}$	287	/	[11]
$MoNb_{12}O_{33}$	321	91.5	[12]
$AlNb_{11}O_{29}$	266	94	[13]
$CrNb_{11}O_{29}$	286	94.7	[15]
$Mg_2Nb_{34}O_{87}$	338	94.8	[16]
$GaNb_{11}O_{29}$	255	96.1	[17]
$FeNb_{11}O_{29}$ nanotubes	273	90.1	[20]
$FeNb_{11}O_{27.9}$	270	90.6	[25]
$FeNb_{11}O_{29}$	262	91.1	This work
$Al_{0.2}Fe_{0.8}Nb_{11}O_{29}$	318	95.0	This work

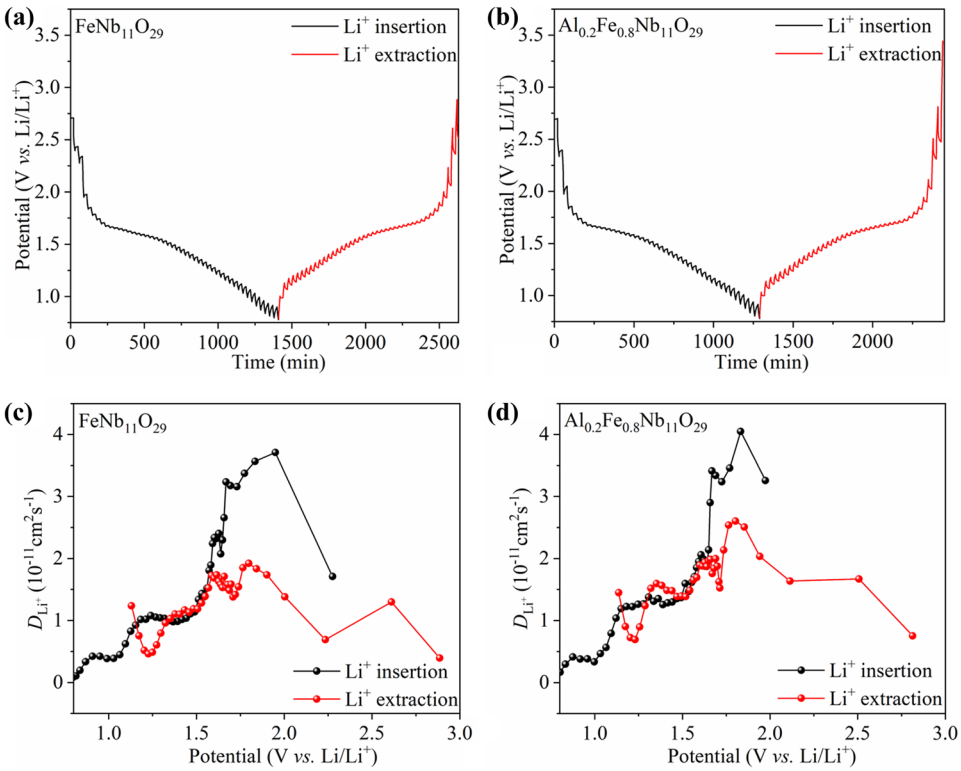

Fig. 6 GITT initial curves of **a** $FeNb_{11}O_{29}$ electrode and **b** $Al_{0.2}Fe_{0.8}Nb_{11}O_{29}$ electrode tested at 0.1C. Calculated D_{Li^+} from GITT curves of **c** $FeNb_{11}O_{29}$ electrode and **d** $Al_{0.2}Fe_{0.8}Nb_{11}O_{29}$ electrode

The structural stability of $Al_{0.2}Fe_{0.8}Nb_{11}O_{29}$ during Li^+ insertion-extraction processes was studied by XRD. Figure 7 demonstrates the XRD results of the fresh $Al_{0.2}Fe_{0.8}Nb_{11}O_{29}$ electrode and the $Al_{0.2}Fe_{0.8}Nb_{11}O_{29}$ electrodes after discharged to 0.8 V as well as charged to 3.0 V in 1st cycle and 10th cycles at 0.1C. It can be found that after the discharge–charge process, no impurity phases (such as Al_2O_3, Fe_2O_3, or Nb_xO_y) appear in the XRD patterns, and no obvious changes are observed in the peak intensities. The XRD patterns of the $FeNb_{11}O_{29}$ electrodes after the similar discharge–charge process are shown in Fig. S5. Very similar results are obtained. Therefore, Al^{3+} doping does not change the crystal structure of $FeNb_{11}O_{29}$ material indeed, and the $Al_{0.2}Fe_{0.8}Nb_{11}O_{29}$ framework is very stable during the electrochemical reaction.

To assess $Al_{0.2}Fe_{0.8}Nb_{11}O_{29}$ practical application value, we prepared a $LiFePO_4/Al_{0.2}Fe_{0.8}Nb_{11}O_{29}$ full cell with $LiFePO_4$ as the cathode material and $Al_{0.2}Fe_{0.8}Nb_{11}O_{29}$ as the anode material. Figure 8a shows the discharge–charge curves of the full cell at 0.1C. It delivered initial-cycle charge/discharge capacities of 241/206 mAh g^{-1}, respectively. Its initial-cycle Coulombic efficiency was 85%. This result is better than the previously reported $LiNi_{0.5}Mn_{1.5}O_4/AlNb_{11}O_{29}$ full cell with charge/discharge capacities of only 238/195 mAh g^{-1} and an initial-cycle Coulombic efficiency of 82% [13]. Figure 8b, c show the discharge–charge curves and rate capability of the $LiPFeO_4/Al_{0.2}Fe_{0.8}Nb_{11}O_{29}$ full cell at different current density from 0.5 to 5C. The discharge capacities are 172, 152, 125, and 83 mAh g^{-1} at 0.5, 1, 2, and 5C, respectively. In particular, compared with the original current density at 0.5C, there is no significant decrease appeared

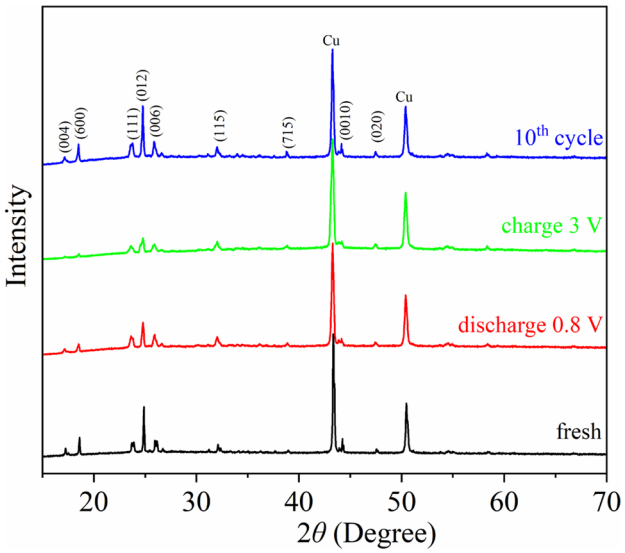

Fig. 7 Ex situ XRD patterns of fresh $Al_{0.2}Fe_{0.8}Nb_{11}O_{29}$ electrode and $Al_{0.2}Fe_{0.8}Nb_{11}O_{29}$ electrodes after discharged to 0.8 V in 1st cycle, charged to 3.0 V in 1st and 10th cycles at 0.1C

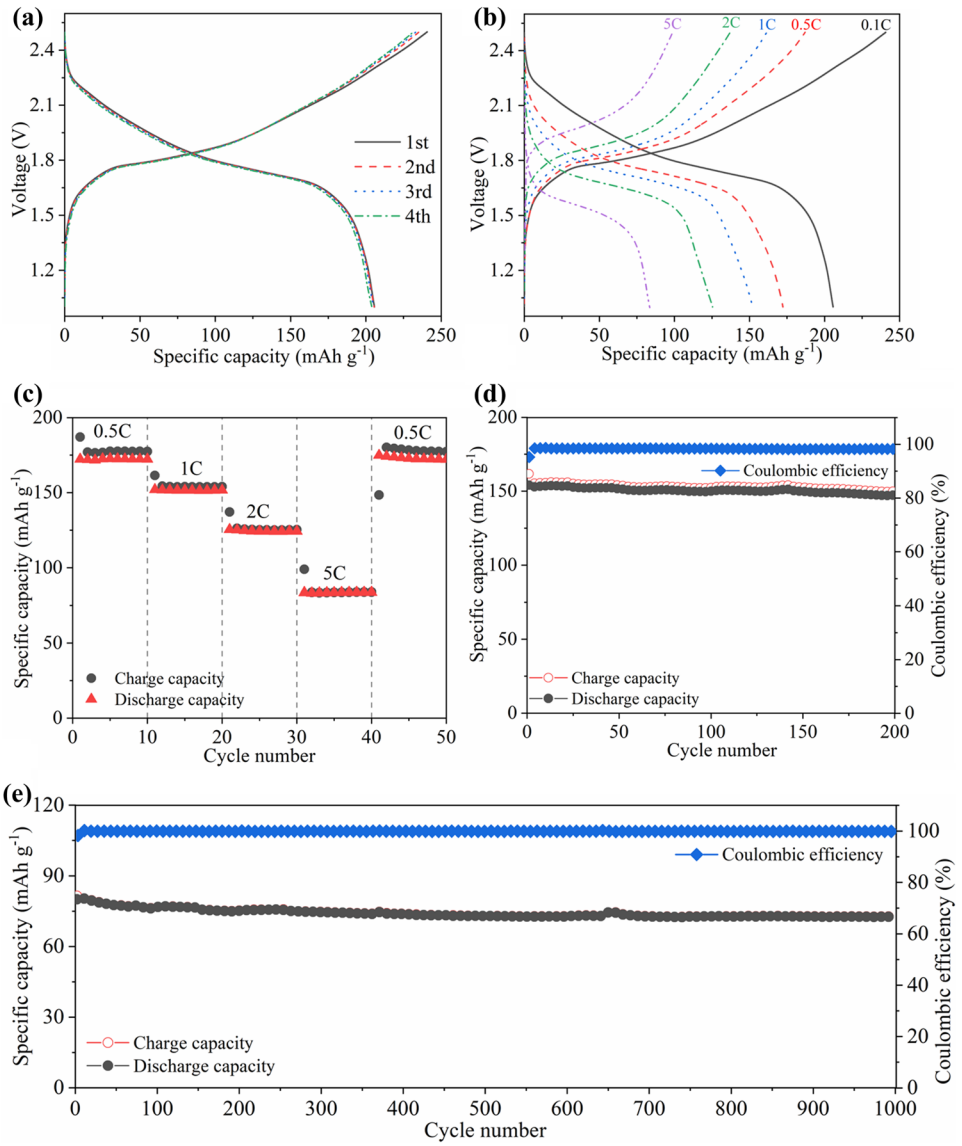

Fig. 8 Electrochemical performance of the $LiFePO_4$/$Al_{0.2}Fe_{0.8}Nb_{11}O_{29}$ full cell: **a** discharge–charge curves at 0.1C, **b** discharge–charge curves at 0.1-5C, **c** rate capabilities, **d** cycling stability at 1C over 200 cycles and Coulombic efficiency, and **e** cycling stability at 10C over 1000 cycles and Coulombic efficiency

in the rate-capability curve when the current density is from 5C back to 0.5C (Fig. 8c). It indicates that the full cell has good electrochemical reversibility. Figure 8d, e show that the capacity retention of the full cell reaches 84.2% after 200 cycles at 1C, and 89.8% after 1000 cycles at 5C, respectively, demonstrating good cycling stability.

4 Conclusions

In summary, the electrochemical performance (especially the specific capacity) of $FeNb_{11}O_{29}$ is improved significantly by doping with Al^{3+}. A reasonable doping amount can preserve the crystal structure, grain size, and morphology of $FeNb_{11}O_{29}$. $Al_{0.2}Fe_{0.8}Nb_{11}O_{29}$ shows improved electrochemical performance, with a reversible capacity of 318 mAh g^{-1} at 0.1 C, high initial-cycle Coulombic efficiency of 95.0%, and relatively high and safe working potential of about 1.61 V. $Al_{0.2}Fe_{0.8}Nb_{11}O_{29}$ further possesses excellent cycling stability with capacity retention of 92.9% over after 1000 cycles. In addition, we assembled a $LiFePO_4$/$Al_{0.2}Fe_{0.8}Nb_{11}O_{29}$ full cell, which also show excellent electrochemical performance. The discharge capacity is up to 206 mAh g^{-1} at 0.1C. The capacity retention of the full cell reaches 84.2% after 200 cycles at 1C, and 89.8% after 1000 cycles at 5C. Therefore, $Al_{0.2}Fe_{0.8}Nb_{11}O_{29}$ may find practical applications in LIBs.

Supplementary information The online version contains supplementary material available at https://doi.org/10.1007/s42114-021-00291-4.

Funding The work is supported by the Natural Science Foundation of Hainan Province (No. 518MS021), High Level Talents Project of Basic and Applied Basic Research Plan of Hainan Province (in Natural Science) (No. 2019RC029), and National Natural Science Foundation of China (No. 51702072).

Declarations

Conflict of interest The authors declare no competing interests.

References

1. Armand M, Tarascon JM (2018) Building better batteries. Nature 451:652–657
2. Dunn B, Kamath H, Tarascon JM (2011) Electrical energy storage for the grid: a battery of choices. Science 334:928–935
3. Ashish AG, Arunkumar P, Babu B, Manikandan P, Sarang S, Shaijumon MM (2015) $TiNb_2O_7$/graphene hybrid material as high performance anode for lithium-ion batteries. Electrochim Acta 176:285–292
4. Augustyn V, Come J (2013) High-rate electrochemical energy storage through Li^+ intercalation pseudocapacitance. Nat Mater 12:518–522
5. Karthick SN, Gnanakan SRP, Subramania A, Kim HJ (2010) Nanocrystalline $LiMn_2O_4$ thin film cathode material prepared by polymer spray pyrolysis method for Li-ion battery. J Alloys Compd 89:674–677
6. Liu Z, Guo RT, Meng JS, Liu X, Wang XP, Li Q, Mai LQ (2017) Facile electrospinning formation of carbon-confined metal oxide cube-in-tube nanostructures for stable lithium storage. Chem Commun 53:8284–8287
7. Zheng SS (2006) The effect of the charging protocol on the cycle life of a Li-ion battery. J Power Sources 161:1385–1391
8. Capsoni D, Bini M, Massarotti V, Mustarelli P, Ferrari S, Chiodelli G, Mozzati MC, Galinetto P (2009) Cr and Ni doping of $Li_4Ti_5O_{12}$: cation distribution and functional properties. J Phys Chem C 113:19664–19671
9. Capsoni D, Bini M, Massarotti V, Mustarelli P, Chiodelli G, Azzoni CB, Mozzati MC, Linati L, Ferrari S (2008) Cations distribution and valence states in Mn-substituted $Li_4Ti_5O_{12}$ structure. Chem Mater 20:4291–4298
10. Zhao XC, Yang P, Ding T, Yang LJ, Mai XM, Chen HY, Wang G, Ma Y, Wang XJ, Murugadoss V, Angaiah S, Wang YP, Liu H, Guo ZH (2019) Hydrothermally synthesized $Li_4Ti_5O_{12}$ nanotubes anode material with enhanced Li-ion battery performances. J Nanosci Nanotechnol 19:7387–7391
11. Li RJ, Qin Y, Liu X, Yang L, Lin CF, Xia R, Lin SW, Chen YJ, Li JB (2018) Conductive $Nb_{25}O_{62}$ and $Nb_{12}O_{29}$ anode materials for use in high-performance lithium-ion storage. Electrochim Acta 266:202–211
12. Zhu XZ, Xu J, Luo YP, Fu QF, Liang GS, Luo LJ, Chen YJ, Lin CF, Zhao XS (2019) $MoNb_{12}O_{33}$ as a new anode material for high-capacity, safe, rapid and durable Li^+ storage: structural characteristics, electrochemical properties and working mechanisms. J Mater Chem A 7:6522–6532
13. Lou XM, Li RJ, Zhu XZ, Luo LJ, Chen YJ, Lin CF, Li HL, Zhao XS (2019) New anode material for lithium-ion batteries: aluminum niobate ($AlNb_{11}O_{29}$). ACS Appl Mater Interfaces 11:6089–6096
14. Fu QF, Li RJ, Zhu XZ, Liang GS, Luo LJ, Chen YJ, Lin CF, Zhao XS (2019) Design synthesis and lithium-ion storage capability of $Al_{0.5}Nb_{24.5}O_{62}$. J Mater Chem A 7 19862–19871
15. Fu QF, Liu X, Hou JR, Pu YR, Lin CF, Yang L, Zhu XZ, Hua L, Lin SW, Luo LJ, Chen YJ (2018) Highly conductive $CrNb_{11}O_{29}$ nanorods for use in high-energy, safe, fast-charging and stable lithium-ion batteries. J Power Sources 379:231–239
16. Zhu XZ, Fu QF, Tang LF, Lin CF, Xu J, Liang GS, Li RJ, Luo LJ, Chen YJ (2018) $Mg_2Nb_{34}O_{87}$ porous microspheres for use in high-energy, safe, fast-charging, and stable lithium-ion batteries. ACS Appl Mater Interfaces 10:23711–23720
17. Lou XM, Fu QF, Xu J, Liu X, Lin CF, Han JX, Luo YP, Chen YJ, Fan XY, Li JB (2018) $GaNb_{11}O_{29}$ nanowebs as high-performance anode materials for lithium-ion batteries. ACS Appl Nano Mater 1:183–190
18. Yang C, Deng SJ, Lin CF, Lin SW, Chen YJ, Li JB, Wu H (2016) Porous $TiNb_{24}O_{62}$ microspheres as high-performance anode materials for lithium-ion batteries of electric vehicles. Nanoscale 8:18792–18799
19. Yang C, Zhang YL, Lv F, Lin CF, Liu Y, Wang K, Feng JR, Wang XH, Chen YJ, Li JB, Guo SJ (2017) Porous $ZrNb_{24}O_{62}$ nanowires with pseudocapacitive behavior achieve high-performance lithium-ion storage. J Mater Chem A 5:22297–22304
20. Zheng RT, Qian SS, Cheng X, Yu HX, Peng N, Liu TT, Zhang JD, Xia MT, Zhu HJ, Shu J (2019) $FeNb_{11}O_{29}$ nanotubes: Superior electrochemical energy storage performance and operating mechanism. Nano Energy 58:399–409
21. Yan L, Shu J, Li CX, Cheng X, Zhu HJ, Yu HX, Zhang CF, Zheng Y, Xie Y, Guo ZP (2019) $W_3Nb_{14}O_{44}$ nanowires: ultrastable lithium storage anode materials for advanced rechargeable batteries. Energy Storage Mater 16:535–544
22. Cheng X, Zhu HJ, Yu HX, Ye WQ, Zheng RT, Liu TT, Peng N, Shui M, Jie S (2018) $K_2Nb_8O_{21}$ nanotubes with superior superior electrochemical performance for ultrastable lithium storage. J Mater Chem A 6:8620–8632
23. Pinus I, Catti M, Ruffo R, Salamone MM, Mari CM (2014) Neutron diffraction and electrochemical study of $FeNb_{11}O_{29}$/$Li_{11}FeNb_{11}O_{29}$ for lithium battery anode applications. Chem Mater 26:2203–2209
24. Lou XM, Xue ZH, Luo ZB, Lin CF, Yang Y, Zhao H, Zheng P, Li JB, Wang N, Chen YJ, Wu H (2017) Exploration of $Cr_{0.2}Fe_{0.8}Nb_{11}O_{29}$ as an advanced anode material for lithium-ion batteries of electric vehicles. Electrochim Acta 245 482–488
25. Lou XM, Lin CF, Luo Q, Zhao JB, Wang B, Li JB, Shao Q, Guo XK, Wang N, Guo ZH (2017) Crystal structure modification enhanced $FeNb_{11}O_{29}$ anodes for lithium-ion batteries. ChemElectroChem 4:3171–3180
26. Zhao ZC, Hu ZQ, Jiao RS, Tang ZH, Dong P, Li YD, Li SD, Li HS (2019) Tailoring multi-layer architectured FeS_2@C hybrids for superior sodium-, potassium- and aluminum-ion storage. Energy Storage Mater 22:228–234
27. Xu BH, Guan XG, Zhang LY, Liu XW, Jiao ZB, Liu XH, Hu XQ, Zhao XS (2018) A simple route to preparing γ-Fe_2O_3/RGO composite electrode materials for lithium ion batteries. J Mater Chem A 6:4048–4054
28. Wu D, Wang C, Wu H, Wang S, Wang F, Chen Z, Zhao T, Zhang Z, Zhang LY, Li CM (2020) Synthesis of hollow Co_3O_4 nanocrystals in situ anchored on holey graphene for high rate lithium-ion batteries. Carbon 163:137–144
29. Li GL, Wang YT, Guo H, Liu ZL, Chen PH, Zheng XY, Sun JL, Chen H, Zheng J, Li XG (2020) Direct plasma phosphorization of Cu foam for Li ion batteries. J Mater Chem A 8:16920–16925
30. Li GL, Wu XQ, Guo H, Guo YR, Chen H, Wu Y, Zheng J, Li XG (2020) Plasma transforming $Ni(OH)_2$ Nanosheets into porous nickel nitride sheets for alkaline hydrogen evolution. ACS Appl Mater Interfaces 12 5951–5957

31. Yang M, Pang MY, Chen JY, Gao FH, Li HL, Guo PZ (2021) Surfactant-assisted synthesis of palladium nanosheets and nanochains for the electrooxidation of ethanol. ACS Appl Mater Interfaces 13:9830–9837
32. Ma N, Wang SQ, Liu XH, Sun YC, Yin YR, Zhang LY, Guo PH (2020) PdPb bimetallic nanowires as electrocatalysts for enhanced ethanol electrooxidation. Sci China Mater 63 2040–2049
33. Li Q, Li HS, Xia QT, Hu ZQ, Zhu Y, Yan SS, Ge C, Zhang QH, Wang XX, Shang XT, Fan ST, Long YZ, Gu L, Miao GX, Yu GH, Moodera JS (2021) Extra storage capacity in transition metal oxide lithium-ion batteries revealed by in situ magnetometry. Nat Mater 20:76–83
34. Li XY, Lin BN, Li HB, Yu Q, Ge Y, Jin X, Liu XH, Zhou YH, Xiao JP (2018) Carbon doped hexagonal BN as a highly efficient metal-free base catalyst for Knoevenagel condensation reaction. Appl Catal B 239:254–259
35. Li Z, Wang C, Chen XZ, Wang XX, Li XY, Yamauchi Y, Xue XJ, Wang J, Lin CF, Luo D, Wang XF, Zhao XS (2020) MoO_x nanoparticles anchored on N-doped porous carbon as Li-ion battery electrode. Chem Eng J 381 122588
36. Subramania A, Angayarkanni N, Vasudevan T (2006) Synthesis of nano-crystalline $LiSr_xMn_{2-x}O_4$ powder by a novel sol-gel thermolysis process for Li-ion polymer battery. J Power Sources 158:1410–1413
37. Subramania A, Angayarkanni N, Gangadharan R, Vasudevan T (2006) Synthesis of nanocrystalline $LiCd_xMn_{2-x}O_4$ cathode materials by using a new combustion fuel for Li-ion polymer battery. Synth React Inorg M 36:203–207
38. Subramania A, Angayarkanni N, Lakshmidevi S, Lakshmidevi R, Gangadharan R, Vasudevan T (2005) A microwave-induced combustion method for the synthesis of nano-crystalline Ni-and Mn-doped $LiCoO_2$ for Li-ion battery. Bull Electrochem 21:411–413
39. Zhao XC, Yang P, Yang LJ, Cheng Y, Guo Z (2018) Enhanced electrochemical performance of Cu^{2+} doped TiO_2 nanoparticles for lithium-ion battery. ES Mater Manuf 1:67–71
40. Yang C, Yu S, Ma Y, Lin CF, Xu ZH, Zhao H, Wu SQ, Zheng P, Zhu ZZ, Li JB, Wang N (2017) Cr^{3+} and Nb^{5+} co-doped $Ti_2Nb_{10}O_{29}$ materials for high-performance lithium-ion storage. J Power Sources 360:470–479
41. Wang MX, Wang K, Huang XB, Zhou T, Xie HS, Ren YR (2020) Improved sodium storage properties of Zr-doped $Na_3V_2(PO_4)_2F_3$/C as cathode material for sodium ion batteries. Ceram Int 46:28490–28498
42. Liang GS, Jin XX, Huang CH, Luo LJ, Chen YJ, Lin CF (2020) Cr^{3+}-doped Li_3VO_4 for enhanced Li^+ storage. Funct Mater Lett 2:2050005
43. Liu Y, Gu YJ, Luo GY, Chen ZI, Wu FZ, Dai XY, Mai Y, Li JQ (2020) Ni-doped $LiFePO_4$/C as high-performance cathode composites for Li-ion batteries. Ceram Int 46 14857–14863
44. Bin M, Quinzeni I, Spada D (2019) The doping of $FeNb_{11}O_{29}$ as a way to improve its electrochemical performance. ChemistrySelect 4:5656–5661
45. Niu C (2018) Al-doped VO_2 (B) nanobelts as cathode material with enhanced electrochemical properties for lithium-ion batteries. Funct Mater Lett 11:1850068
46. Madhavi S, Rao GS, Chowdari B, Li S (2001) Effect of aluminium doping on cathodic behaviour of $LiNi_{0.7}Co_{0.3}O_2$. J Power Sources 93 156–162
47. Wang JL, Li ZH, Yang J, Tang JJ, Yu JJ, Nie WB, Lei GT, Xiao QZ (2012) Effect of Al-doping on the electrochemical properties of a three-dimensionally porous lithium manganese oxide for lithium-ion batteries. Electrochim Acta 75:115–122
48. Ding Y, Xie J, Cao G, Zhu T, Yu H, Zhao X (2011) Enhanced elevated-temperature performance of Al-doping single-crystalline $LiMn_2O_4$ nanotubes as cathodes for lithium-ion batteries. J Phys Chem C 115:9821–9825
49. Jang YI, Moorehead WD, Chiang YM (2002) Synthesis of the monoclinic and orthorhombic phases of $LiMnO_2$ in oxidizing atmosphere. Solid State Ionics 149:201–207
50. Zhan D, Liang Y, Cui P, Xiao Z (2015) Al-doped $LiMn_2O_4$ single crystalline nanorods with enhanced elevated-temperature electrochemical performance via a template-engaged method as a cathode material for lithium-ion batteries. RSC Adv 5:6372–6377
51. Larson AC and Von Dreele RB (2004) General Structure Analysis System (GSAS), Los Alamos National Laboratory report LAUR. 86–748
52. Toby BH (2001) EXPGUI, a graphical user interface for GSAS. J Appl Crystallogr 34:210–213
53. Li X, Huang YY, Li YY, Sun SX, Liu Y, Luo JH, Han JT (2017) Al doping effects on $LiCrTiO_4$ as an anode for lithium-ion batteries. RSC Adv 7:4791–4797
54. Wadsley AD (1961) Mixed oxides of titanium and niobium. II. The crystal structures of the dimorphic forms $Ti_2Nb_{10}O_{29}$. J Acta Crystallogr 14 664–670
55. Do SJ, Santhoshkumar P, Kang SH, Prasanna K, Jo YN, Lee CW (2019) Al-doped $Li[Ni_{0.78}Co_{0.1}Mn_{0.1}Al_{0.02}]O_2$ for high performance of lithium ions batteries. Ceram Int 45 6972–6977